Highly absorption and an excellent optical bandgap of CuO doped Fe nanoparticles for advanced photocatalytic applications

S. Bagyalakshmi[a], M. Subash[a], R. Uthrakumar[a,*], S. Aravindan[b], K. Kaviyarasu[c,d]
[a]*Department of Physics, Govt. Arts College (Autonomous), Salem - 636007, Tamil Nadu, India*
[b]*Department of Physics, Chikkanna Government Arts College, Tirupur - 641602, Tamil Nadu, India*
[c]*UNESCO-UNISA Africa Chair in Nanosciences/Nanotechnology Laboratories, College of Graduate Studies, University of South Africa (UNISA), Muckleneuk Ridge, PO Box 392, Pretoria, South Africa*
[d]*Nanosciences African Network (NANOAFNET), Materials Research Group (MRG), iThemba LABS-National Research Foundation (NRF), 1 Old Faure Road, 7129, PO Box 722, Somerset West, Western Cape Province, South Africa*

The sol-gel technique can be used to fabricate purified copper (II) oxide (CuO) and doped Fe nanoparticles. Synthesized nanostructures were examined using XRD, FTIR, UV-visible spectroscopy, SEM-EDX, and vibrating sample magnetometer to determine their crystalline nature, shape, surface area, and elemental composition. Under visible light illumination, photocatalytic evaluations of methylene blue (MB) dye degradation with binary metal oxides were conducted to evaluate the catalyst's recyclability. The photocatalytic degrading of the MB dye pollutant by CuO nanoparticles doped Fe has been shown in detail experiments under visible light irradiation.

1. Introduction

There are many transition metal oxides (TMOs) with monoclinic assemblies, including copper (II) oxide (CuO), and these exhibit a very narrow bandgap about 1.21 - 1.5 eV. The availability and affordability of CuO have made it a popular semiconductor in recent years for gas sensors due to its potential applications. Among its many applications are solar energy conversion processes, lithium-ion electrode materials, magnetic materials, and photocatalysts [3, 4]. CuO's characteristics may be altered by doping this with transition metals including Ni, Zn, Fe, Al, and Mn, allowing it to be used in more sophisticated implementations [5-8]. Various forms of nanomaterials have been used to fabricate various topologies of CuO nanomaterials, including nanoparticles, nanorods, nanowires, nanoplates, and nanotubes [9, 10].

Also, Cu has three oxidation states: Cu^+, Cu^{2+}, and Cu^{3+}, which allow *p*-type and *n*-type doping [11-14]. As a result of changing CuO's electron density, metal doping alters its optical, electrical, and magnetic properties. The literature contains numerous papers on Fe doped CuO nanostructures, including solute-gel studies [15] and hydrothermal [16] are two examples of hydrothermal methods yielding Fe doped CuO nanoparticles. Moreover, semiconductor nanoparticles are currently commonly used in the removal of different organic dyes [17-21]. The CuO nanoparticles have an outstanding role in photocatalysis using visible irradiation among the various semiconductor metal oxide photocatalyst. There have been reports of significant air pollution caused by methylene blue (MB) dye, in particular. As a result, in recent years, cationic and anionic dyes have been widely employed in a wide range of industries, including textile and ceramic manufacturing; printing; medicines; leather manufacture; cosmetics; and hair-colouring.

In this work, we propose to prepare nanocomposite materials with different elements in different amounts by using a simple sol-gel technique and examine how additives affect their characteristics. Consequently, the purpose of this study is to describe how CuO doped Fe nanostructures can be made using a sol-gel process, and how Fe concentration can be analyzed for XRD, SEM-EDX, FTIR, and UV-vis spectroscopy to determine their crystallite dimension, shape, chemical bonding, and bandgap. In order to plot the magnetic characteristics of these nanoparticles, we utilize a vibration sample magnetometer (VSM). Several experimental conditions were examined, including the concentration of MB, absorption, and photodegradation efficiency of the CuO/Fe nanostructure, in the study of photocatalyst. Study findings indicate that the CuO/Fe material is a potential material for practical use.

2. Experimental procedure

The formation of pure copper oxide nanostructures was carried out using analytical grade chemicals, 0.4 M copper nitrate [$Cu(NO_3)_2$] and 0.4 M sodium hydroxide (NaOH) mixed in double distilled water (dd-H_2O) and vigorously stirred with a magnetic stirrer. Following that, a sodium hydroxide blend is mixed droplet by droplet with copper nitrate solution, while mixing constantly. This same technique is used in the production of CuO doped Fe nanostructures that contain 0.01 M% of Fe concentrations. The copper nitrate and sodium hydroxide mixed with ferric nitrate (Fe $(NO_3)_3.4H_2O$) 0.4 M% are synthesised into CuO doped Fe nanoparticles by vigorously stirring them for 3 hrs in double distilled water (dd-H_2O). As the copper nitrate and iron nitrate mixtures are well mixed, sodium hydroxide is added drop by drop while stirring continually. Water and twice distilled ethanol are used to rinse the solution several times. The dried residue is sintered at 300°C for 7 hours after being maintained in the muffle furnace. The samples generated satisfied the structural, morphological, and optical requirements for structural, morphological, and optical studies by using XRD, UV-vis, FTIR, scanning electron microscopy (SEM), and energy dispersive X-ray spectrometry (EDX). The vibrating sample magnetometer (VSM) and the analysis of photocatalytic activity were described in detail.
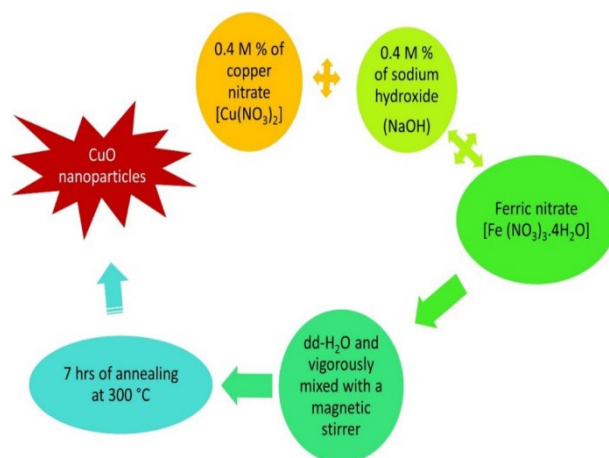

Fig. 1. This chart illustrates the process of synthesizing pure CuO and doped Fe nanoparticles.

3. Results and discussion

3.1 XRD analysis

A powder XRD technique was used to determine the crystallite size, phase, and crystalline nature of synthesised samples. Figure shows the XRD patterns for pure & doped Fe nanoparticles with different amounts of Fe in the 20º - 80º range as shown in Fig. 2. The peaks correspond to the surfaces labelled in 16.2º, 23.6º, 29.5º, 32.8º, 34.5º, 38.7º and 52.1º. Lattice planes (110), (111),

(202), (211), (220), (-111), and (222) are all represented by peaks, it was verified that CuO doped Fe NPs were present because of their crystallographic orientation, which matched the information on the JCPDS card (48-1548) [22]. Using the experimental data, CuO nanoparticles are found to have lattice parameters a = 4.6876 Å, b = 3.4104 Å, and c = 5.1138 Å, with a monoclinic structure. By using the Debye-Scherer equation (1), we calculate the mean crystallite size of pure CuO and doped Fe by assessing the Full-Width Half-Maximum (FWHM) at the best prominence at 38.93° as; $D = 0.9\lambda/\beta cos\theta$; When the form factor is 0.9, the X-ray wavelength, FWHM, and Bragg's angle of reflection are calculated. According to a Debye Scherrer calculation [23], the mean crystal size of CuO nanoparticles in the CuO/Fe system is 9.6 nm, whereas the mean crystal size of CuO nanoparticles in the CuO/Fe system.
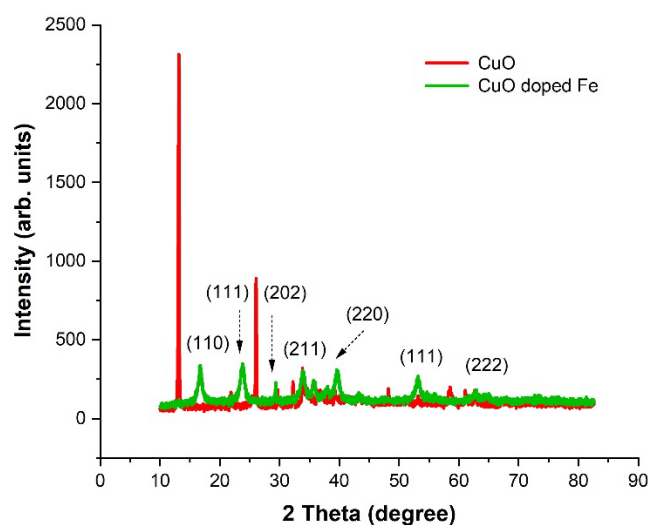

Fig. 2. An XRD pattern of pure CuO and nanoparticles doped with Fe ions

Table 1. Using CuO nanoparticles and doped with Fe, an analysis of peak position and grain size was conducted.

Peak position 2θ (deg)	Miller Indices (hkl)	θ of the intense peak (deg)	FWHM of intense peak β (radius)	Size of the particle D (nm)
16.2	110	0.990023	0.016483	8.493
23.6	111	0.978867	0.016927	8.364
29.1	202	0.967928	0.017385	8.236
32.8	211	0.959313	0.017693	8.165
34.5	220	0.955019	0.018026	8.051
38.7	111	0.943512	0.018413	7.977
52.1	222	0.898411	0.018753	8.226

3.2. FTIR analysis

Infrared Fourier Transform spectroscopy (FTIR) is among the most effective methods for investigating structural features because it provides pertinent information about the phase structure of the material as well as how different types of polymers are connected [24]. In Fig. 3 we show the FTIR signatures of pure CuO nanoparticles and nanoparticles doped with Fe ions. A wide-range band region of 3600 cm^{-1} - 3250 cm^{-1} was produced by the O-H bending of CuO-linked water molecules. There is an O-H bending vibration of the CuO hydroxyl group at 3441 cm^{-1}, which is responsible for the strong and wide absorbance spike at this wavelength. H$_2$O, O-H bending modal oscillations are attributed to the absorbance maxima at 1642 cm^{-1} and 1443 cm^{-1}

[26, 27]. CuO nanoparticles doped Fe displayed three distinct IR absorption bands for their Cu-O oscillations at 881 cm^{-1}, 603 cm^{-1}, and 504 cm^{-1}, as initially reported [28].
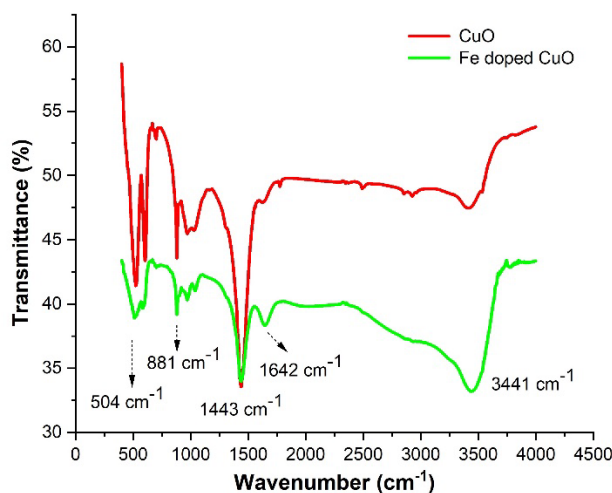

Fig. 3. The FTIR spectrum of pure CuO and Fe nanoparticles.

3.3. UV-visible spectra of CuO nanoparticles

The UV-visible absorbance of a substance can be calculated by analyzing how its absorbency changes as a function of frequency and wavelength. A UV-visible spectrophotometer measures both wavelengths of absorption and the intensity of absorption at each wavelength. The absorbance of UV-visible light can be seen in Fig. 4(a). Doped Fe nanoparticles and copper oxide exhibit strong absorbance at 238 nm and 246 nm, respectively. By analyzing the UV-visible absorption spectrum of manufactured nanoparticles, the characteristics of their absorption have been analyzed, since the optical characteristics of nanoparticles can change according to their size, structure, concentration, and others. Copper oxide nanoparticles' energy gap (E_g) can be calculated using this approach. The *Tauc plot* of Cu doped Fe nanoparticles as shows in Fig. 4(b) an optical bandgap of 5.13 eV. Thus, it is evident that depending on the dopant introduced into CuO matrix, its bandgap can be tuned.
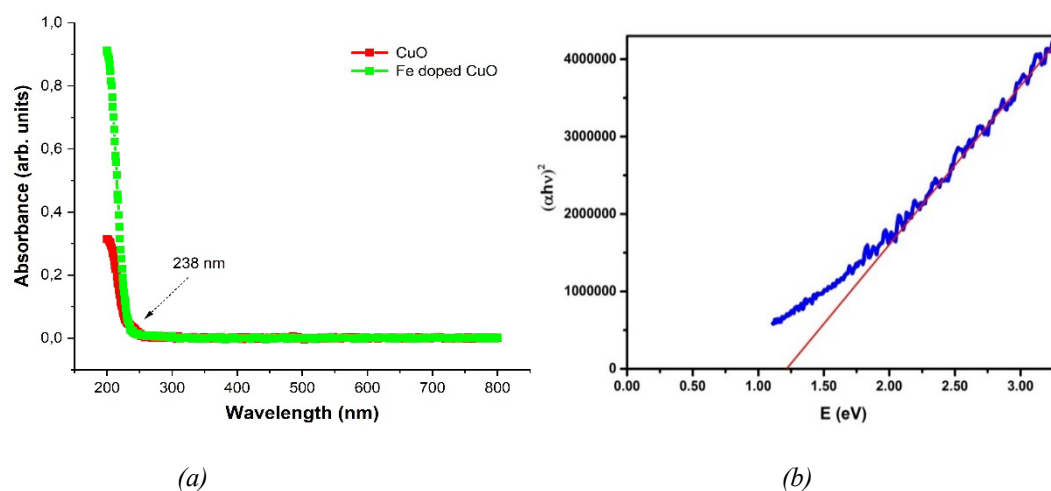

(a)   *(b)*

Fig. 4 (a). The UV-vis absorption spectrum of pure CuO and doped Fe nanoparticles; (b) Tauc plot relation of CuO doped Fe nanoparticles.

3.4. Morphological Study (SEM-EDX)

A combination of SEM and energy dispersive X-rays was used to evaluate the morphological changes in pure and Fe doped nanoparticles (SEM-EDX). Copper oxide (CuO) nanoparticles that have been produced and those that have been doped with iron are pictured in Fig. 5(a-b) as sphere-shaped entities. Different factors can affect the geometry of nanostructures, including response time, doping level, synthesis technique, etc. As a result of the EDX assessment, the results are shown in Fig. 5(c-d). It is evident from the EDX spectrum that several well-defined spikes are related to CuO and Fe, which indicates that CuO doped Fe nanoparticles are present, it is inevitable that everything will connect in Fig. 5(a-d). A spectra analysis did not reveal any peaks related to contaminants, correlating that the particles synthesized were CuO doped Fe nanoparticles. The EDX elements of atomic and weight percentage values has been tabulated in Table 2.
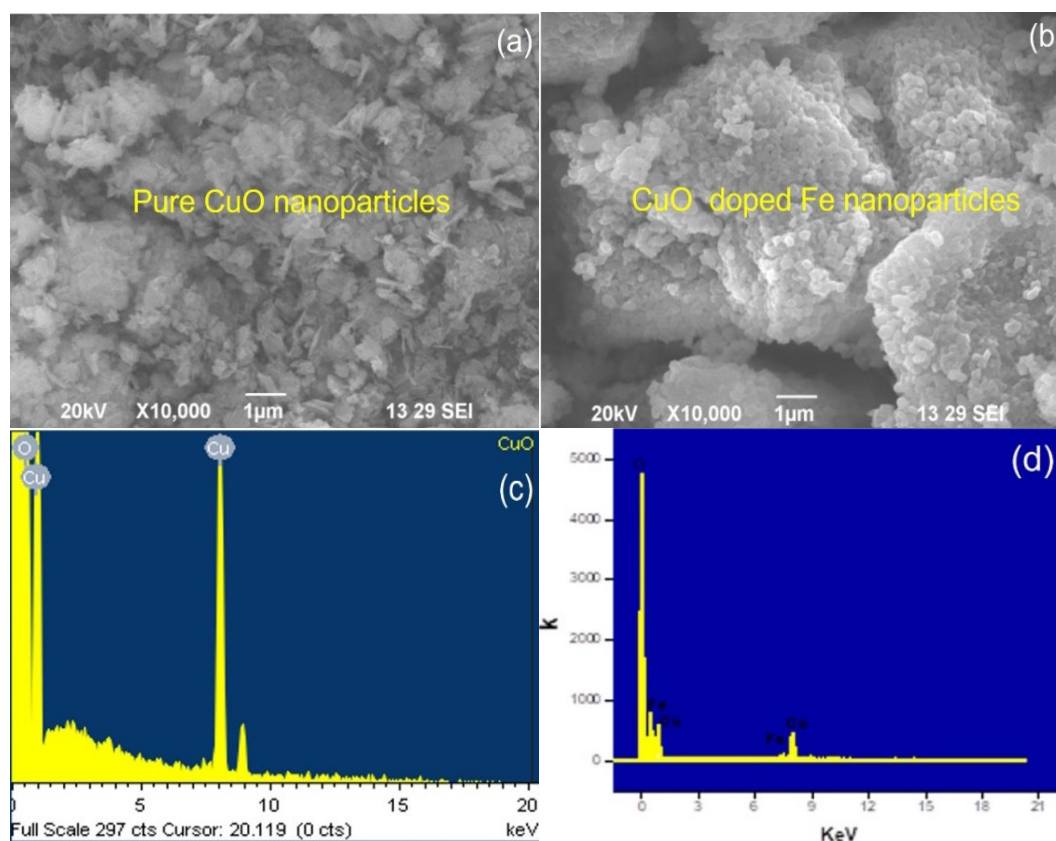

Fig. 5. (a-d). SEM and EDAX spectrum of pure CuO and doped Fe nanoparticles.

Table 2. Aspects of the composition of Fe nanoparticles doped with CuO.

CuO doped Fe nanoparticles: chemical composition		
Elements	Weight % keV	Atomic %
Cu	37.48	50.34
Na	6.50	1.33
O	47.76	45.76
Fe	8.26	2.57
Total	100.00	

3.5. Dielectric studies

Crystallinity variations may be studied using the dielectric properties of these materials. As a result, dielectric tests on CuO nanomaterial were performed using the HIOKI 3532-50 LCR HITESTER. The specified films were deposited with conductive silver paste to improve the ohmic contact and then were coated with fine-grade alumina powder to provide a better surface quality. The dielectric constant is determined using this approach.

$$\varepsilon = \frac{cd}{A\varepsilon_0}$$

(2)

The intrinsic permittivity of empty space, 8.854×10^{-12} F/m, is represented by the constants c, d, A, and 0. There was a correlation between this relationship and the resulting theoretical dielectric constant.

$$\varepsilon^{'} = \varepsilon \tan \delta$$

(3)

It can be seen from the graph in Fig. 6(a) that the dielectric constant and dielectric dissipation factors of a formed crystal decrease as the frequency rises at ambient temperature. A material's dielectric constant is determined by the influence of different polarizations (*electronic, atomic, ionic, space charge, and so on*) that develop in the material when it is exposed to electric field changes. The high dielectric constant at low frequencies is due to the presence of charge density polarisation. Various polarizations have a distinct effect on the wavelength - dependent dielectric permittivity. It is crucial for magnetic applications that a material's dielectric loss Fig. 6(b) be low at high frequencies since this implies that the material has superior magnetic characteristics and has fewer defects.
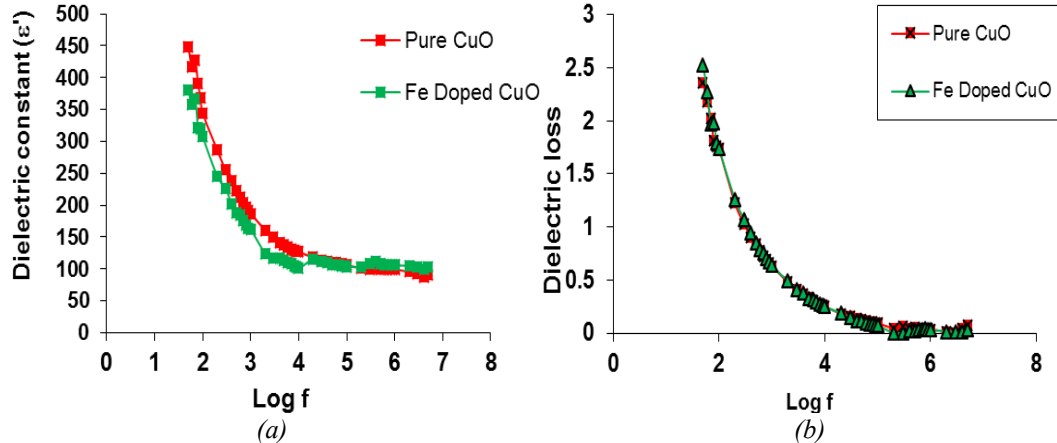

Fig. 6. (a) Dielectric constant vs log f; (b) Dielectric loss vs log f.

3.6. Magnetic properties

The hysteresis loop between magnetization and magnetic field established for the nanostructures at ambient temperature is shown in Fig. 7. CuO NPs exhibit paramagnetic behaviour at ambient temperature, and mild ferromagnetic activity due to the paramagnetic transition. Borzoi *et al.*, observed similar magnetic behaviour at room temperature for nano sized cupric oxide produced using a ball-milling procedure [29]. At ambient temperature, hysteresis loops were discovered for pure CuO, and Fe doped nanoparticles using an oscillating sample magnetometer, as illustrated in Fig. 7. Because of the crystallite size *d*=39.67 nm, pure CuO exhibits super paramagnetic behaviour in present case. The magnetic capacities explicate the super paramagnetic and increased magnetic moments observed are produced by the presence of uninsured surface spins of CuO nanoparticles. [30-33].
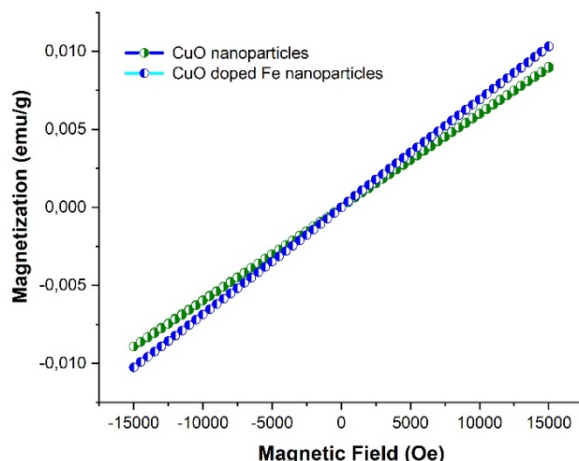
Fig. 7. Magnetization curve of pure CuO and Fe doped nanoparticles.

3.7. Photocatalytic measurements

Copper oxide nanoparticles, which have a high optical absorption and an excellent bandgap, are one of the most promising choices for application as a photocatalytic material in the breakdown of organic contaminants. The fluctuation in the absorbance of the MB solution in the presence of pure CuO and doped Fe nanoparticles under visible light irradiation for 120 minutes and 140 minutes is shown in Fig. 8(a-b). Changes in the strength of the MB dye's distinctive absorbance peak at 663 nm were used to quantify the dye's degradation. The MB degradation rate decreases with reaction time in the presence of CuO and doped Fe catalysts, indicating that nanoparticles have excellent photocatalytic activity. The photocatalytic degradation efficiency of as produced CuO is 84% after 120 minutes. The pseudo-first-order model was used to investigate the reaction kinetics of MB dye using equation (4).

$$\ln (C_t/C_o) = kt \tag{4}$$

where, C_o is the dye concentration at the start of the experiment, C_t is the dye concentration at various irradiation times, and 'k' is the photodegradation rate constant $(\min^{-1})$ [34, 35]. As demonstrated in Fig. 9(a) and Fig. 9(b), the linear fit between $\ln (C_t/C_o)$ and the reaction time of MB dye follows pseudo-first-order kinetics behaviour. The values of rate constant 'k' were denoted by Table 3.
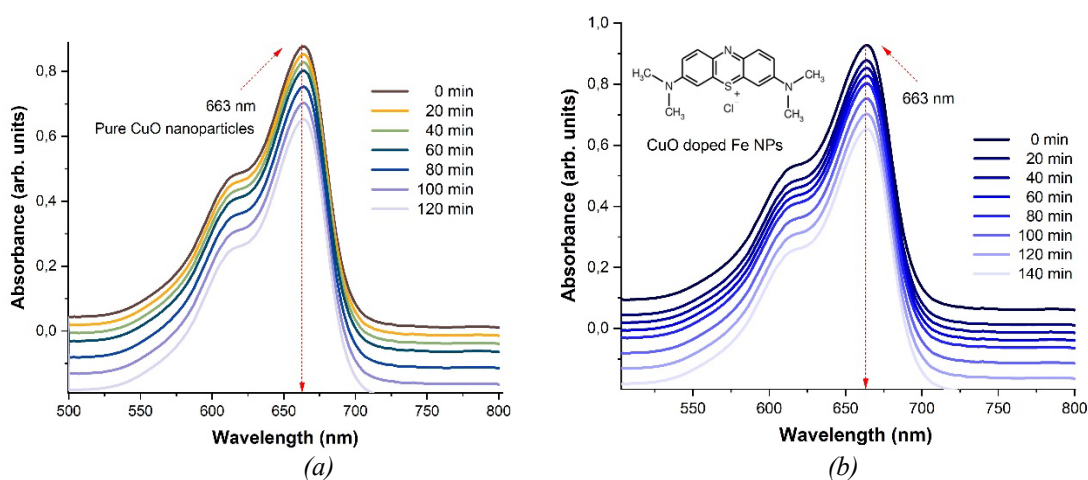

(a)   *(b)*

Fig. 8. (a) UV absorption spectra of using pure CuO nanoparticles; (b) UV absorption spectra of using CuO doped Fe nanoparticles.
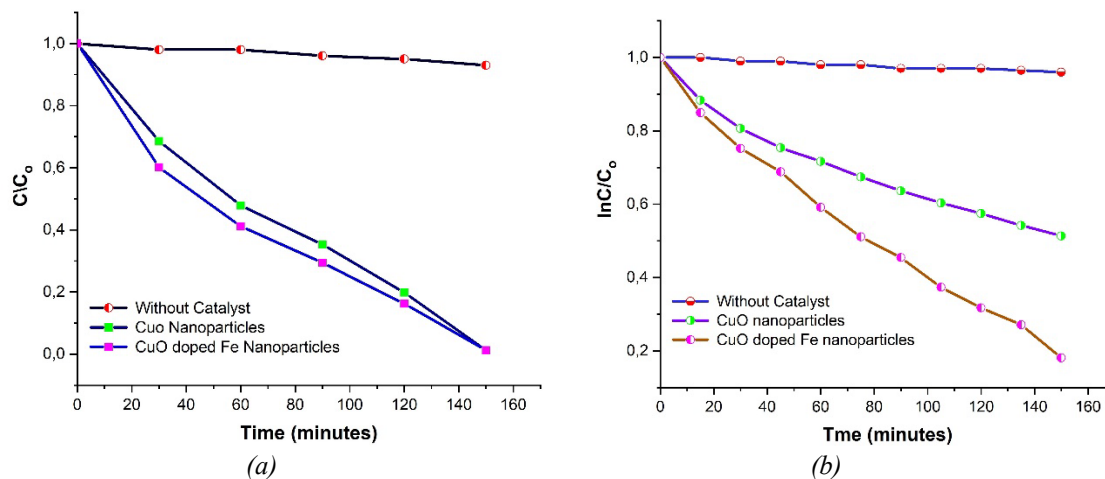
Fig. 9. (a) Absorption, photolysis, and sunlight photocatalytic activity of pure CuO and Fe doped nanoparticles; (b) In (C_t/C_o) versus irradiation time for MB degradation using pure CuO and Fe doped nanoparticles.

Table 3. The value of photodegradation rate constant (min^{-1}).

S. No	Composition	In(C/C_o)	Time (min)	K = In (C/C_o)/t (min^{-1})
1.	CuO	0.75	133	0.0056390
2.	Fe-CuO	0.75	151	0.0049668
3.	Without catalyst	1.0	152	0.0065789

The photostability for MB degradation with efficiencies of 84%, 74%, 64%, 44%, 34%, for five cycles respectively. These findings may be attributed to the CuO and Fe doped nanoparticles' chemical stability, as seen in Fig. 10.
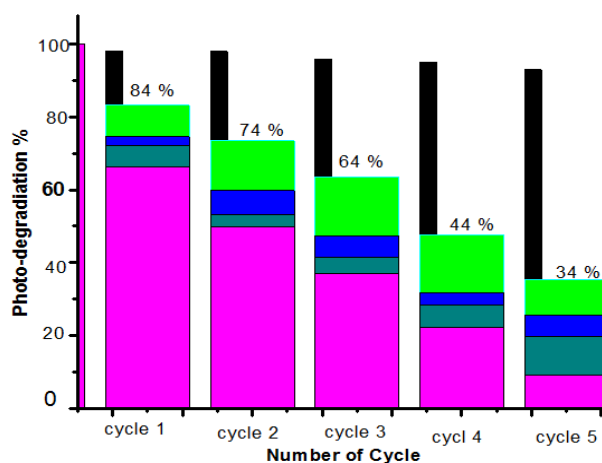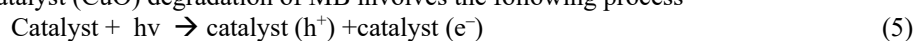

Fig. 10. The photodegradation efficiency of the number of cycles.

The photocatalytic process is based on the activation of CuO and Fe doped nanoparticles by visible light, which results in the generation of free active radicals such OH-, O_2^-, and H_2O^- species.

Catalyst (CuO) degradation of MB involves the following process

$$\text{Catalyst} + \text{hv} \rightarrow \text{catalyst (h}^+\text{)} + \text{catalyst (e}^-\text{)} \tag{5}$$

$$\text{Catalyst (e}^-) + O_2 \rightarrow \text{catalyst} + O_2^- \tag{6}$$
$$\text{Catalyst (h}^+) + H_2O \rightarrow \text{catalyst} + OH^- + H^+ \tag{7}$$
$$\text{Catalyst (h}^+) + OH^- \rightarrow + OH \tag{8}$$
$$\text{Dye} + (O_2^- ; OH^-) \rightarrow \text{intermediates} \rightarrow \text{degradation products} \tag{9}$$
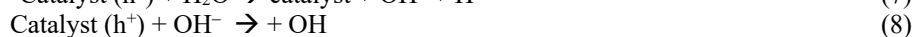
The photogenerated electron hole pair process, which involves the trapping of electrons by oxygen to create super oxide species (O_2), is explained by equations (5) - (9). -OH is formed as a result of the reaction, and hydroxyl radicals are created as a result of accepting the holes [36-38]. The reaction mechanism was taken place in the photocatalytic activity of the CuO doped Fe nanoparticles photocatalyst under visible light is presented in Fig. 11.
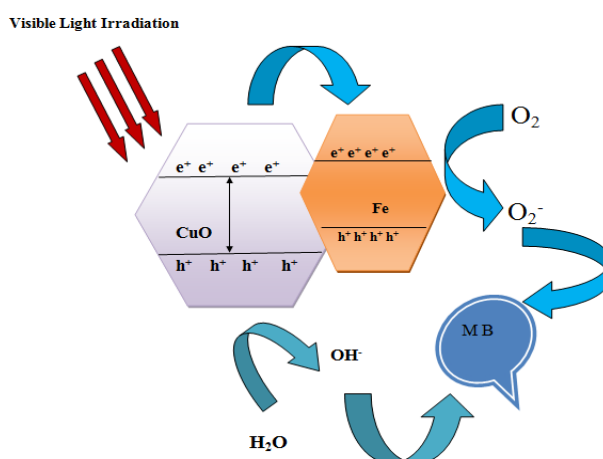

Fig. 11. Diagram for photocatalytic degradation mechanism of pure CuO and Fe doped nanoparticles

4. Conclusion

To summarize, chemical precipitation methods have been used to create pure CuO and Fe doped nanostructures. The monoclinic crystalline structure of pure CuO and Fe doped nanoparticles is confirmed by X-ray diffraction investigation. The frequencies of pure CuO nanoparticles showed three distinct IR absorption bands for Cu-O band oscillations at 603 cm^{-1}, 497 cm^{-1}, & 432 cm^{-1}. The UV-visible spectrophotometer records the sharp absorption at 230 nm and 240 nm due to copper oxide and Fe doped CuO nanoparticles. Structural examination of SEM images reveals that the nanoparticles are spherical in form and somewhat aggregated. Several well-defined peaks in the EDX spectra were evidently related to CuO and Fe, indicating that the Fe doped CuO nanoparticles. At ambient temperature, the electromagnetic characteristics show that the dielectric constant and dielectric dissipation decline frequency. The specimens' magnetic hysteresis loops revealed that the nanostructures are super-paramagnetic in nature. Photocatalytic investigations have shown that pure and Fe doped CuO nanoparticles have excellent photocatalytic properties. After 140 minutes of visible light irradiation, the produced nanostructures showed strong photocatalytic activity for dissolving the MB dye, with a percentage degradation of roughly 84%. The improved photocatalytic activity is attributed to the combined influence of excitons e^-/h^+ pair recombination, crystallinity, and active surface area. It's also can be used for pollutant degradation and other applications linked to the environment.

210

References

[1] 1Q. Zhang, K. Zhang, D. Xu, G. Yang, H. Huang, Prog. Mater. Sci. 60, 208, (2014); https://doi.org/10.1016/j.pmatsci.2013.09.003

[2] S. Logambal, C. Maheswari, S. Chandrasekar, T. Thilagavathi, C. Inmozhi, S. Panimalar, F.A. Bassyouni, R. Uthrakumar, Mohamed Ragab Abdel Gawwad, Reem M. Aljowaie, Dunia A. Al Farraj, K. Kanimozhi, J. King Saud Uni. - Sci., 34, (3), 101910, (2022); https://doi.org/10.1016/j.jksus.2022.101910

[3] S. Panimalar, M. Chandrasekar. S. Logambal, R. Uthrakumar, C. Inmozhi, Materials Today: Proceedings, 56, 3394, (2022); https://doi.org/10.1016/j.matpr.2021.10.335

[4] S. Panimalar, S. Logambal, R. Thambidurai, C. Inmozhi, R. Uthrakumar, Azhaguchamy Muthukumaran, Rabab Ahmed Rasheed, Mansour K. Gatasheh, A. Raja, J. Kennedy, K. Kaviyarasu, Environmental Research, 205, 112560, (2022); https://doi.org/10.1016/j.envres.2021.112560

[5] T. Kida, T. Oka, M. Nagano, Y. Ishiwata, and X. G. Zheng, Journal of the American Ceramic Society, 90, 107 , (2007); https://doi.org/10.1111/j.1551-2916.2006.01402.x

[6] A. Ganguly, O. Anjaneyulu, K. Ojha, A.K. Gangul. Cryst. Eng. Comm. 17, 8978 (2015) https://doi.org/10.1039/C5CE01343G

[7] X. Chen, S. Carabineiro, S. Bastors, P. Tavares, J. Orfoo, M. Pereira, J. Figueiredo, J. Environment chem.Rev.113, 4391, (2013)

[8] S.M. Yakout, A.M. El-Sayed, Advanced powder Technology. 08, 033, (2019),

[9] P. Lu. W. Zhou, Y. Li, J. Wang, P. Wu, Ceram. Int.43, 9798, (2017); https://doi.org/10.1016/j.ceramint.2017.04.159

[10] J. Saad Mabrouk Yakout, Opt. Mater. 0925, 3467, (2020)

[11] A.S. Ehiraj, D.J. Kang, Nanoscale Res. Lett. 7, 1, (2012); https://doi.org/10.1186/1556-276X-7-70

[12] R. Manimaran, K. Palaniradja, N. Alagumurthi, S. Sendhilnathan, J. Hussain, Applied Nanoscience, 4, 163, (2014); https://doi.org/10.1007/s13204-012-0184-7

[13] J. Albadi, A. Mansournezhad and H. Abbaszadeh, Journal of the Chinese Chemical Society, 60, 1193, (2013); https://doi.org/10.1002/jccs.201300178

[14] Amal George, D. MagimaiAntoni Raj, A. Dhayal Raj, A. Albert Irudayaraj, J. Arumugam, H. Joy Prabu, S. John Sundaram, Naif Abdullah Al-Dhabi, MariadhasValan Arasu, M. Maaza, K. Kaviyarasu, Surfaces and Interfaces 21, 100761, (2020); https://doi.org/10.1016/j.surfin.2020.100761

[15] G.T. Anand, S.J. Sundaram, K. Kanimozhi, R. Nithiyavathi, K. Kaviyarasu, Materials Today: Proceedings 36, 427, (2021); https://doi.org/10.1016/j.matpr.2020.04.881

[16] R. Nithiyavathi, S. John Sundaram, A. Al Farraj Dunia, Abdel Gawwad Mohamed Ragab, Y. Samson, K. Kaviyarasu, Journal of Infection and Public Health, 14, 1893, (2021); https://doi.org/10.1016/j.jiph.2021.10.022

[17] N.M. Basith, J.J. Vijaya, L.J. Kennedy, M. Bououdina, Physica E 53 193, (2013); https://doi.org/10.1016/j.physe.2013.05.009

[18] V. Perumal, A. Sabarinathan, M. Chandrasekar, M. Subash, C. Inmozhi, R. Uthrakumar, Abdulgalim B. Isaev, A. Raja, Mohamed S. Elshikh, Saeedah Musaed Almutairi, K. Kaviyarasu, Fuel, 324, 124599, (2022); https://doi.org/10.1016/j.fuel.2022.124599

[19] M Subash, M Chandrasekar, S Panimalar, C Inmozhi, K Parasuraman, R Uthrakumar, K Kaviyarasu, Biomass Conv. Bioref. 12, 1, (2022)

[20] V. Perumal, C. Inmozhi, R. Uthrakumar, R. Robert, M. Chandrasekar, S. Beer Mohamed, Shehla Honey, A. Raja, Fahd A. Al-Mekhlafi, K. Kaviyarasu, Environmental Research, 209, 112821, (2022); https://doi.org/10.1016/j.envres.2022.112821

[21] S. Panimalar, M. Subash, M. Chandrasekar, R. Uthrakumar, C. Inmozhi, Wedad A. Al-Onazi, Amal M. Al-Mohaimeed, Tse-Wei Chen, J. Kennedy, M. Maaza, K. Kaviyarasu, Chemosphere, 293, 133646, (2022); https://doi.org/10.1016/j.chemosphere.2022.133646

[22] Z. Zhou, C. Lu, X. Wu and X. Zhang, RSC Advances, 3, 26066, (2013); https://doi.org/10.1039/c3ra43006e

[23] B.P. Singh. M. Chaudhary, A. Kumar, A.K. Singh, Y.K. Gautam, S. Rani, R. Walia, Solid State Sci. 106, 106296, (2020); https://doi.org/10.1016/j.solidstatesciences.2020.106296

[24] J.P. Joshua, S. Krishnan, D. Raj, R. Uthrakumar, S. Laxmi and S.J. Das, International Journal of Chem. Tech Research, 6, 22, (2014)

[25] G. Yuan, H. Jiang, C. Lin, S. Liao, J. Cyst. Growth, 303, 400, (2007); https://doi.org/10.1016/j.jcrysgro.2006.12.047

[26] S Panimalar, R Uthrakumar, E Tamil Selvi, P Gomathy, C Inmozhi, K Kaviyarasu, J Kennedy, Surfaces and Interfaces 20, 100512, (2020); https://doi.org/10.1016/j.surfin.2020.100512

[27] M. Chandrasekar, S. Panimalar, R. Uthrakumar, M. Kumar, M.E. Raja Saravanan, G. Gobi, P. Matheswaran, C. Inmozhi, K. Kaviyarasu, Materials today proceeding. 36, 228, (2021); https://doi.org/10.1016/j.matpr.2020.03.228

[28] A.S. Ethiraj, D.J. Kang, Nanoscale Res. Lett. 7, 1, (2012); https://doi.org/10.1186/1556-276X-7-70

[29] R.A Boriz, S.J. Stewart, R.C. Mercader, G. Punte, F. Garcia, J. Magn. Magn. Mater. 226, 1513, (2001); https://doi.org/10.1016/S0304-8853(00)00943-4

[30] D. Saravanakkumar, Hicham Abou Oualid, Younes Brahmi, A. Ayeshamariam, M. Karunanaithy, A. Mohamed Saleem, K. Kaviyarasu, S. Sivaranjani, M. Jayachandran, Open Nano 4, 100025, (2019); https://doi.org/10.1016/j.onano.2018.11.001

[31] Sowmya Sri Rathnakumar, Kana Noluthando, Arockia Jayalatha Kulandaiswamy, John Bosco Balaguru Rayappan, Kaviyarasu Kasinathan, John Kennedy, Malik Maaza, Sensors and Actuators B: Chemical 293, 100, (2019); https://doi.org/10.1016/j.snb.2019.04.141

[32] M. Chandrasekar, M. Subash, V. Perumal, S. Panimalar, S. Aravindan, R. Uthrakumar, C. Inmozhi, Abdulgalim B. Isaev, Sudhakar Muniyasamy, A. Raja, K. Kaviyarasu Separation and Purification Technology, 294, 121189, (2022); https://doi.org/10.1016/j.seppur.2022.121189

[33] M. Chandrasekar, M. Subash, S. Logambal, G. Udhayakumar, R. Uthrakumar, C. Inmozhi, Wedad A. Al-Onazi, Amal M. Al-Mohaimeed, Tse-Wei Chen, K. Kanimozhi, J. King Saud Uni. - Sci., 34, (3), 101831, (2022); https://doi.org/10.1016/j.jksus.2022.101831

[34] N. Kana, K. Kaviyarasu, T. Khamliche, C.M. Magdalane, M. Maaza, Journal of Environmental Chemical Engineering 7 (4), 103255, (2019); https://doi.org/10.1016/j.jece.2019.103255

[35] R. Saravanan, S. Karthikeyan, V.K. Gupta. G. Sekran, V. Narayanan, A. Stephen, Mater, Sci. Eng, C33, 91, (2013); https://doi.org/10.1016/j.msec.2012.08.011

[36] H. Fang. Y. Guo, T. Wu, Y, Liu, New J. Chem. 42, 12779, (2018); https://doi.org/10.1039/C8NJ02052C

[37] K. Kaviyarasu, C.M. Magdalane, K. Anand, E. Manikandan, M. Maaza, Spectrochimica Acta Part A: Molecular and Biomolecular Spectroscopy 142, 405, (2015); https://doi.org/10.1016/j.saa.2015.01.111

[38] R. Thambidurai, G. Gobi, R. Uthrakumar, C. Inmozhi, K. Kaviyarasu, Digest Journal of Nanomaterials & Biostructures, 18(3), 869, (2023); https://doi.org/10.15251/DJNB.2023.183.869